mater.scichina.com link.springer.com

Published online 13 October 2023 | https://doi.org/10.1007/s40843-023-2623-x
Sci China Mater 2023, 66(11): 4207–4219

SPECIAL TOPIC: High-performance Structural Materials

Ultra-strong metal/high entropy alloy nanolaminates: Utilizing size constraining effects on phase transformation

Yufang Zhao, Yaqiang Wang*, Jinyu Zhang*, Kai Wu, Gang Liu and Jun Sun*

ABSTRACT **In this work, the phase stability of non-equiatomic $Fe_{50}Mn_{30}Co_{10}Cr_{10}$ and $Fe_{50}Mn_{30}Co_{10}Ni_{10}$ high entropy alloys (HEAs) under strong constraining conditions as well as its effect on the mechanical properties were comparatively studied in the magnetron sputtered Cu/$Fe_{50}Mn_{30}Co_{10}Cr_{10}$ and Cu/$Fe_{50}Mn_{30}Co_{10}Ni_{10}$ nanolaminates with the layer thickness *h* ranging from 5 to 150 nm. During the deposition process, the size-driven hexagonal close packed (HCP) to face-centered cubic (FCC) phase transformation occurs in the $Fe_{50}Mn_{30}Co_{10}Cr_{10}$ layers as $h < 25$ nm due to the nanolayer constraining and template effects. Meanwhile, the stress-driven HCP-to-FCC phase transformation also occurs in the Cu/$Fe_{50}Mn_{30}Co_{10}Cr_{10}$ nanolaminates during the indentation deformation, which is attributed to the nucleation of stacking faults that could serve as the nuclei for phase transformation. However, the $Fe_{50}Mn_{30}Co_{10}Ni_{10}$ layers maintain stable microstructure without size-driven nor stress-driven phase transformation. With reducing *h*, both the Cu/HEA nanolaminates exhibit a transition from *h*-independent to *h*-dependent ultrahigh hardness, as elucidated by the partial dislocation-mediated mechanisms. In particular, the normalized hardness of Cu/$Fe_{50}Mn_{30}Co_{10}Cr_{10}$ nanolaminates represented by the ratio of measured hardness to predicted hardness from the rule-of-mixture is more superior to conventional Cu-based bimetal nanolaminates. These findings provide a new perspective to tailor the phase transformation of HEAs and thereby enhance their strength and plasticity.**

Keywords: metal/high entropy alloy nanolaminates, phase transformation, hardness, interfaces, size effects

INTRODUCTION

Outstanding toughness is one of the most essential and desired properties in structural materials, which is always hardly achieved because the strength and ductility are usually mutually exclusive [1,2]. A new class of metallic materials, i.e., high entropy alloys (HEAs), opening a new avenue to design high-performance materials, have attracted intensive attention during the past decade owing to their excellent properties [3,4]. Their excellent mechanical properties, such as superior strength [5,6], large ductility [7,8] and good fatigue resistance [9], are often explained by different plastic mechanisms based on ordinary dislocation slip and/or deformation twinning. Recently, the stress-driven phase transformation, generally observed in transformation-induced plasticity (TRIP) steels [10], has been unveiled in bulk HEAs, e.g., FeMnCoCr [11] and TaHfZrTi HEA [12]. The phase transformation-mediated plasticity enables the dual-phase $Fe_{50}Mn_{30}Co_{10}Cr_{10}$ (FMCC) HEA [11] to show simultaneous enhancement in strength and ductility, due to a combination of the duplex microstructure-induced interface hardening [13] and the face-centered cubic (FCC) to hexagonal close packed (HCP) phase transformation hardening. Specifically, stacking faults (SFs) formed by the gliding of Shockley partials can act as the nuclei of the HCP phase that forms *via* the gliding of <112>/6 partials on every other {111} plane [14,15]. Interestingly, a bidirectional TRIP effect has also been uncovered in the FMCC HEAs, showing the stress-driven FCC-to-HCP transformation and reversion under both reversed cyclic loading [15] and uniaxial tensile loading [16]. However, prior studies mainly focused on the transformable bulk non-equiatomic HEAs [11,17]. As their grain sizes decrease to nanoscale, how the microstructure and mechanical properties evolve in nanocrystalline HEAs is still mysterious.

In parallel, the unique design concept and physical (thermal, mechanical, and anticorrosive) properties give these small-scaled HEAs often with nanocrystalline microstructures great potential applications in functional barriers/coatings, thin-film-resistors, and electronic products [18]. Prior studies have demonstrated that the ductility and strength of a material can also be controlled by scaling, i.e., the sample and microstructural sizes [19]. On the one hand, cracking becomes more difficult in small-sized materials, i.e., good plasticity could be obtained, even in conspicuous classes of brittle materials [20]. On the other hand, materials can realize significantly increased strength by reducing their dimensions due to the limited length of dislocation sources [21]. The nanostructured HEA thin films can reach high strength on the order of a few gigapascals [22], but their main drawback is that the microstructure easily coarsens due to the high mobility of grain boundaries (GBs), consequently degrading the long-term mechanical properties. To achieve even higher strength associated with stabilized nanocrystalline structures, a popular methodology is introducing abundant heterogeneous interfaces to suppress the grain growth in HEA thin films, e.g., synthesizing the structures of nano-dual-phase thin films [23] or nanolaminates (NLs) [24].

In these metallic NLs composed of alternating soft/hard nanolayers, the heterogeneous interfaces play critical roles in

State Key Laboratory for Mechanical Behavior of Materials, Xi'an Jiaotong University, Xi'an 710049, China
* Corresponding authors (emails: yaqiangwang@xjtu.edu.cn (Wang Y); jinyuzhang1002@xjtu.edu.cn (Zhang J); junsun@xjtu.edu.cn (Sun J))

their mechanical behavior *via* serving as dislocation sources/sinks/barriers [25,26]. Previous studies have verified that these metallic NLs possessed excellent properties due to their unique microstructures, such as high strength and ductility [25,27], superior radiation tolerance [28], and great thermal stability [29]. The strong size-constraining effect in NLs not only affects their layer thickness h-dependent phase transformation behavior [30,31], but also the h-dependent mechanical properties and strengthening mechanisms [32,33]. Specifically, the coherent interfaces with good strain compatibility but weak barriers for slip transmission of dislocations due to continuous slip systems confer the metal/HEA NLs, e.g., Cu/FeCoCrNi [34] and Ni/FeCoCrNi [35], unique deformation behavior and outstanding mechanical properties. In this scenario, it is natural to quest how the size-constraining effect influences the phase transformation of FMCC HEA nanolayered constituents as well as the mechanical responses of metal/HEA NLs.

By far, some experiments [36] and atomistic simulations [37] have shown that the FeMnCoCrNi system possessed low SF energy (SFE), which was even predicted to be negative at 0 K. The SFE has an influence on the plastic deformation mechanisms, including the ordinary dislocation slip, deformation twinning and phase transformation, therefore impacts the mechanical properties of HEAs [38]. In fact, lowering the SFE in FeMnCoCrNi HEAs can be achieved by adding elements, e.g., Fe [39], or reducing elements, e.g., Ni [40]. Moreover, Co acts as a stabilizer for the FCC phase in the Fe-Co binary system [41], and thus the reduction in Co contents results in reduced phase stability of non-equiatomic HEAs. This facilitates the formation of the dual-phase microstructure, further leading to notable phase transformation strengthening. For example, both FMCC [11] and $Ta_{0.5}HfZrTi$ [12] HEAs exhibit enhanced mechanical properties compared with their equiatomic siblings with higher phase stability. Therefore, to explore the SFE effect on phase stability, we engineer the soft Cu phase with the hard nanocrystalline FMCC and $Fe_{50}Mn_{30}Co_{10}Ni_{10}$ (FMCN) HEA phase to construct the Cu/FMCC and Cu/FMCN NLs, so as to investigate the size constraining effects on the microstructural evolution of FMCC and FMCN HEA phase and the coherent interface-dominant mechanical properties of NLs.

Taken together, here we comparatively investigated the microstructural evolution and strengthening mechanisms in Cu/FMCC and Cu/FMCN metal/HEA NLs. Compared with their bulk counterparts, the as-deposited FMCC nanolayers in Cu/HEA NLs exhibited the h-dependent phase microstructure, i.e., the FCC + HCP dual-phase microstructure at large h but FCC single phase at small h, while that of FMCN nanolayers maintained the single FCC phase as the bulk. During the nanoindentation tests, the dual-phase FMCC layers exhibited the stress-driven HCP-to-FCC phase transformation, while the single-phase FMCN nanolayers were difficult to transform. This study may provide a new perspective to manipulate the phase transformation of HEAs *via* heterogeneous coherent interfaces in strong constraining NLs.

EXPERIMENTAL SECTION

Alternative Cu/FMCC and Cu/FMCN NLs with the total thickness of ~1.5 μm were deposited on HF-etched (111)-Si wafers by direct current magnetron sputtering at room temperature. The individual layer thickness h in both kinds of Cu/HEA NLs was equal and varied from ~5 to ~150 nm. Pure Cu (99.995 wt%), FeMnCoCr (99.95 wt%, atomic percentage in sequence was Fe: 56%, Mn: 22.3%, Co: 10.3% and Cr: 11.4%, respectively) and FeMnCoNi (99.95 wt%, atomic percentage in sequence was Fe: 56.8%, Mn: 22.6%, Co: 10.4% and Ni: 10.2%, respectively) targets were used to prepare the NLs. The sputtering chamber was evacuated to a base pressure of 4×10^{-4} Pa before the deposition process and Ar pressure of 1 Pa was maintained during the preparation process. The first layer deposited on the substrate was always the Cu, and the cap layer was the HEA.

To identify the phase structures and crystallographic orientations of film materials, X-ray diffraction (XRD) experiment was carried out on a Bruker D8 Discover powder X-ray diffractometer with Cu Kα radiation at room temperature. Transmission electron microscopy (TEM) analysis was performed on a JEOL JEM-2100F microscope with 200 kV accelerating voltages to observe the internal features before and after indentation. The TEM specimens of Cu/HEA NLs after indentation were prepared by the lifting out technique by means of a Helios Nano Lab 600i dual-beam focused ion beam (FIB) system. Energy-dispersive X-ray (EDX) analyses were carried out to determine the elemental composition using an Oxford Instruments EDX detector with a spatial resolution of ~1 nm for chemical analysis.

Nanoindentation tests were conducted on the Cu/HEA NLs using a TI950 TriboIndenter (Hysitron, Minneapolis) equipped with a standard Berkvoich diamond indenter at room temperature according to the Oliver–Pharr method [42]. The data were acquired within a maximum indentation depth of ~10%–15% of the total film thickness for each specimen to avoid the substrate effect. The nanoindentation was carried out under the load-controlled mode with the maximum loads of 4500 and 5000 μN for Cu/FMCC and Cu/FMCN NLs, respectively. A minimum of nine indents separated each other at least 25 μm were performed on each sample to acquire the average hardness with the standard deviations. Before testing, drift monitor/correction was performed to improve the accuracy of data. More details can be referred to our previous work [34].

RESULTS

Microstructures of the as-deposited Cu/HEA NLs

Fig. 1 presents the high-angle XRD spectra for these two kinds of the as-deposited Cu/HEA NLs. One can see that the Cu peaks and HEA peaks overlap each other owing to their same lattice structure and similar lattice parameters. The features of diffraction peaks of Cu/FMCC NLs in Fig. 1a show the size-dependence with a critical layer thickness h_c ~25 nm. (i) In the Regime-I with h < 25 nm, Cu/FMCC NLs exhibit the single FCC structure with strong (111), weak (200) and (220) peaks. (ii) In the Regime-II with $h \geqslant 25$ nm, the HCP (0002) and ($10\bar{1}3$) peaks of FMCC layers gradually appear, whose intensity increases with increasing h. By contrast, Cu/FMCN NLs only show FCC (111), (200) and (220) peaks without the existence of HCP peaks, see Fig. 1b.

Figs 2 and 3 display the representatively cross-sectional TEM images of the as-deposited Cu/FMCC and Cu/FMCN NLs with different h, respectively. It appears that the morphologies of the microstructure can be divided into two regimes by a critical layer thickness h_c = 25 and 50 nm for Cu/FMCC and Cu/FMCN NLs, respectively. The main results are summarized as follows.

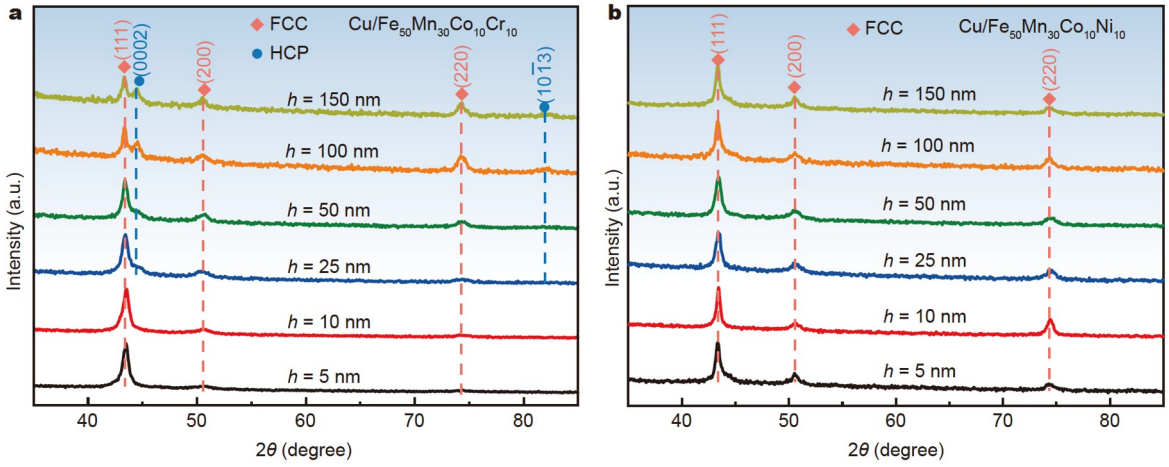

Figure 1 XRD patterns of (a) Cu/FMCC and (b) Cu/FMCN NLs with different layer thicknesses.

(i) In Regime-I with $h < h_c$, the Cu/HEA interfaces cannot be identified in the bright field TEM images and a columnar grain along the growth direction contains several interfaces, while the scanning TEM (STEM)/EDX results display the nanolayered structure clearly, as shown in Figs 2b and 3b. Chemical compositions obtained from the EDX of the present HEA nanolayers are summarized in Table 1, showing that the atomic ratio of both FMCC and FMCN layers is about 5:3:1:1, consistent with our design. The selected area diffraction patterns (SADPs) in Figs 2a and 3a, d show the overlapping diffraction rings and the single FCC structure of these two Cu/HEA NLs, which is in accordance with the XRD results. In addition, the nanotwins in the columnar grains penetrate the interfaces (termed as penetrated twins), as shown in Figs 2c and 3c, e, f for Cu/FMCC and Cu/FMCN NLs, respectively.

(ii) In Regime-II with $h \geqslant h_c$, the layered structure and interfaces are clear in the bright field TEM images and the nanotwins are confined inside the isolated layers (termed as confined twins), as shown in Fig. 2d–h for Cu/FMCC NLs and Fig. 3g–i for Cu/FMCN NLs. For Cu/FMCC NLs, the HCP phase appears in the FMCC layers, which is revealed by overlapping $\{\bar{1}11\}_F$&$\{0002\}_H$, $\{220\}_F$&$\{11\bar{2}0\}_H$ diffraction rings and individual HCP $\{10\bar{1}2\}_H$, $\{10\bar{1}3\}_H$ rings, see the SADPs in Fig. 2d–f and g–i for h = 25 and 100 nm samples, respectively. Meanwhile, the fast Fourier transform (FFT) images also manifest the dual-phase structure of FMCC layers. The microstructural morphology of Cu/FMCC NLs with h = 25 nm exhibits a transition feature from Regime-I to Regime-II, in which the grains near the surface behave as the internal morphology in the Regime-I and those close to the substrate exhibit the morphology in Regime-II. By contrast, Cu/FMCN NLs in Regime-II also exhibit single FCC structure, see Fig. 3g–i. The 9*R* phase, comprised of an SF ribbon consisting of a repeated unit of 9{111} atomic layers [43], emerges in FMCN layers. Moreover, the high-resolution TEM (HRTEM) observations show that the interfaces are coherent without misfit dislocations, see Fig. 3i.

Figs 4 and 5 show the histogram of grain size d-distribution and that of twin spacing λ-distribution in Cu/FMCC NLs and Cu/FMCN NLs, respectively. The microstructural sizes, including the grain size d, the twin spacing λ, and the number fraction of twinned grain P, are summarized in Figs 4c, f and 5e, f, respectively. It appears that the microstructural sizes in the Regime-I of Cu/HEA NLs are insensitive to h. The in-plane grain size d of Cu and HEA layers almost keeps a constant of ~30 nm. The λ of both Cu/HEA NLs is nearly equal ~5.5 nm and the P remains unchanged ~61% in Cu/FMCC NLs and ~72% in Cu/FMCN NLs. In Regime-II, all these microstructural sizes of Cu layers increase with increasing h, while the grain size d of HEA layers is still insensitive to h. The λ of individual HEA layers is absent in Fig. 5e and the P of HEA layers is ~100% in Fig. 5f, considering it is difficult to identify their specific values due to the vast planar defects (e.g., nanotwins and SFs) in their every extremely tiny grains.

Microstructures of indented Cu/HEA NLs

To elucidate the deformation behavior and underlying mechanisms, post-mortem TEM observations were performed on the indented Cu/HEA NLs with different h, as shown in Figs 6 and 7. It is revealed that the constituent layers behave homogenous thinning in the severely deformed region (under the indenter tip) without highly localized shear bands in both kinds of Cu/HEA NLs. In addition, since both Cu and HEA layers behave a significant reduction of layer thickness after nanoindentation tests, both of them make great contributions to the plastic deformation.

For the Cu/FMCC NLs with h = 10 nm in Regime-I, they maintain the initial crystallographic orientations after deformation, implying that no phase transformation occurs during nanoindentation, as shown in Fig. 6b. A local magnified TEM image of the boxed region in Fig. 6a displays that nanotwins still exist after deformation, as indicated by the orange arrows in Fig. 6c. It implies these nanotwins in both Cu and HEA layers are stable and no detwinning occurs. The penetrated nanotwins were also observed in HRTEM image, see Fig. 6d. By contrast, for Cu/FMCC NLs with h = 25 and 100 nm in Regime-II, the HCP $\{10\bar{1}3\}_H$ ring disappears after deformation, as revealed in Fig. 6f, j, respectively. It is suggested that the HCP to FCC phase transformation occurs in FMCC nanolayers. Also, the nanotwins in Cu and FMCC layers still exist after nanoindentation, as indicated in Fig. 6g, h and k, l, implying that detwinning does not occur and the nanotwins are stable during deformation.

For the Cu/FMCN NLs regardless of h, it appears that the diffraction rings in SADPs of the as-deposited samples on the left and indented samples on the right are the same, demon-

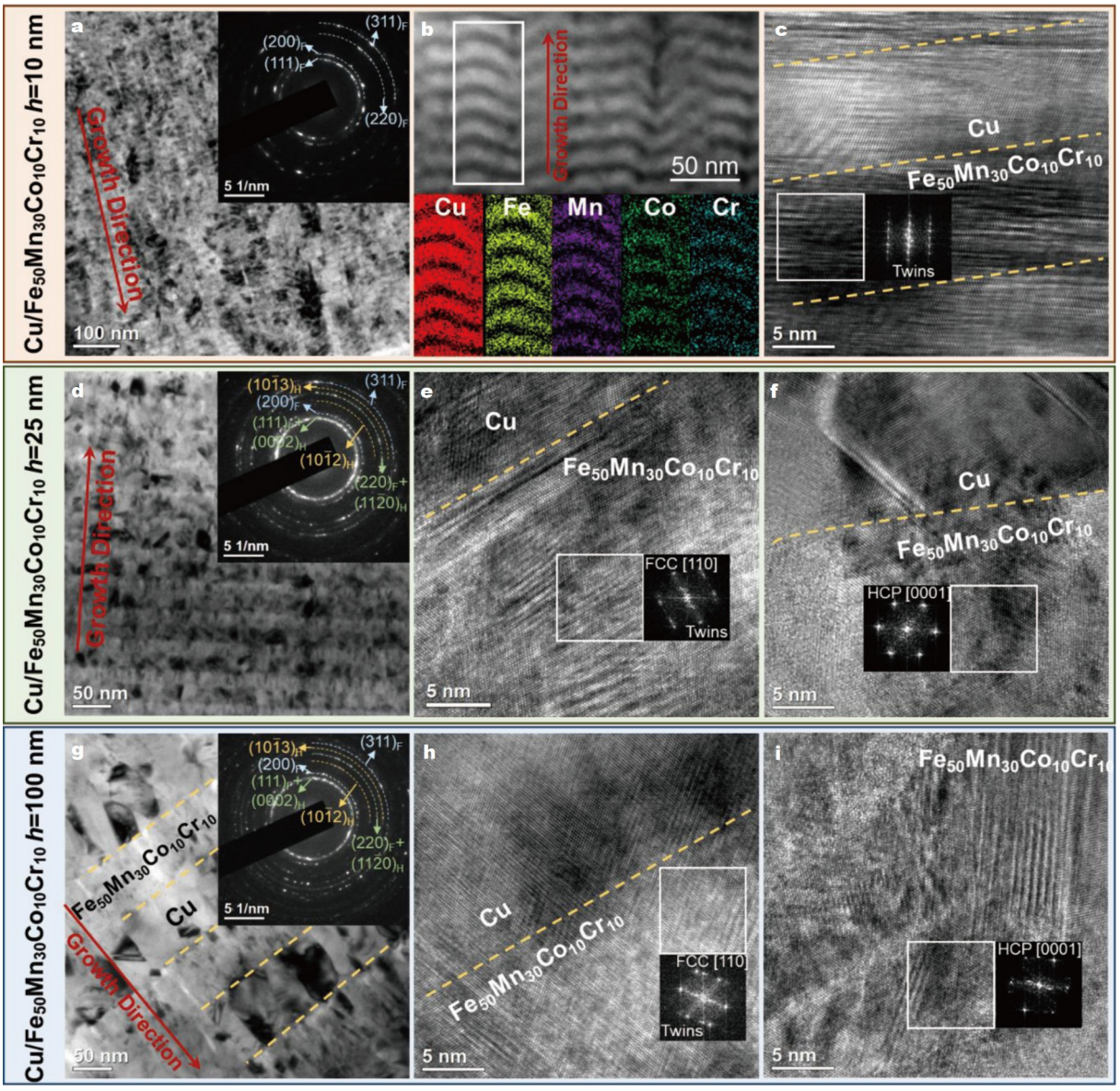

Figure 2 (a) Representative TEM image of Cu/FMCC NLs with h = 10 nm. (b) Corresponding STEM image and EDX mapping analysis, showing clearly modulated nanolayered structure. (c) Typical HRTEM image of Cu/FMCC NLs with h = 10 nm. (d) Typical TEM image of Cu/FMCC NLs with h = 25 nm, and (e, f) its corresponding HRTEM images, showing the dual-phase structure in FMCC layers. (g) Typical TEM image of Cu/FMCC NLs with h = 100 nm, and (h, i) its corresponding HRTEM images. The corresponding SADPs are inserted in (a, d, g).

strating the remained single FCC structure after nanoindentation, see Fig. 7b, f. The deformation behaviors in the two regimes (samples with different h) are similar. No phase transformation occurs and the nanotwins in both Cu and FMCN layers are stable, as shown in Fig. 7b–d and f–h for Cu/FMCN NLs with h = 25 nm in Regime-I and h = 100 nm in Regime-II, respectively.

Mechanical properties of Cu/HEA NLs

Fig. 8a displays the typical indentation load-displacement curves of the two Cu/HEA NLs with different h at a strain rate of 0.1 s^{-1}. The indentation depth of Cu/HEA NLs firstly remains constant with reducing h from 150 to 50 nm, then gradually decreases as h further decreases. The h-dependent indentation hardness of the two Cu/HEA NLs is shown in Fig. 8b. The hardness tendencies of the two Cu/HEA NLs are similar, and both of them behave a hardness plateau and then increase with reducing h. In Regime-I, the hardness of Cu/FMCC NLs increases from ~4.3 to ~4.8 GPa with reducing h from 25 to 5 nm, and that of Cu/FMCN NLs monotonically increases from ~3.8 to ~4.6 GPa as h decreases from 50 to 5 nm. In Regime-II, both Cu/FMCC and Cu/FMCN NLs show a hardness plateau of ~3.8 GPa.

To further estimate the influence of HEA and stress-induced transformation on the strengthening of multilayers, we introduced the parameter of normalized hardness, H/H_{ROM}, to represent their strengthening capability, where H_{ROM} was calculated *via* the rule of mixture (ROM). Fig. 8c summarizes the hardness of the present Cu/HEA NLs and the reported conventional Cu-based bimetal NLs as a function of $h^{-1/2}$ [33,35,44–46]. Obviously, the strengthening capability of NLs containing

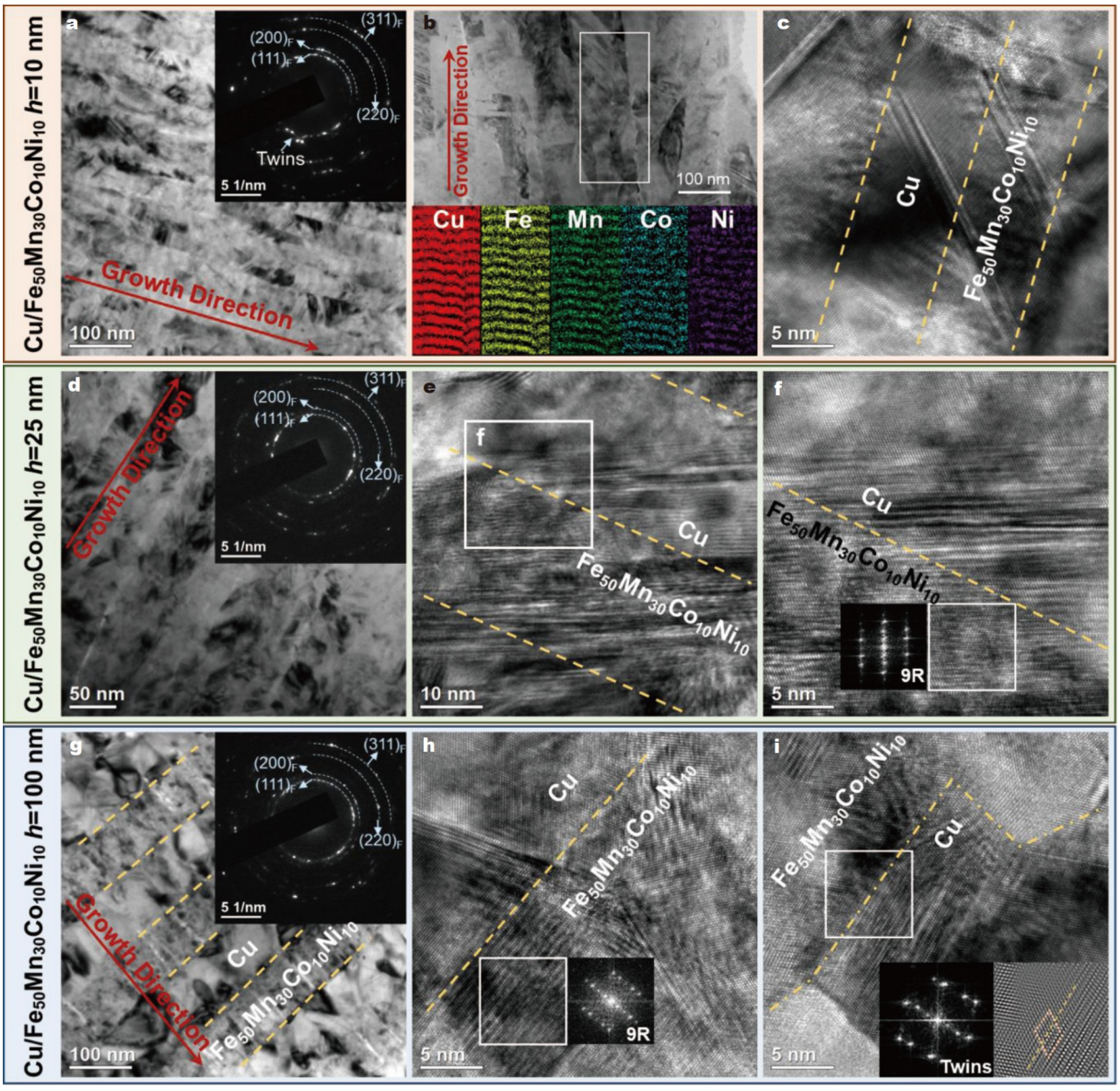

Figure 3 (a) Representative TEM image of Cu/FMCN NLs with h = 10 nm. (b) Corresponding STEM image and EDX mapping analysis, showing clearly modulated nanolayered structure. (c) Typical HRTEM image of Cu/FMCN NLs with h = 10 nm. (d) Typical TEM image of Cu/FMCN NLs with h = 25 nm, and (e, f) its corresponding HRTEM images. (g) Typical TEM image of Cu/FMCN NLs with h = 100 nm, and (h, i) its corresponding HRTEM images. The corresponding SADPs are inserted in (a, d, g).

Table 1 Chemical compositions of the present FMCC and FMCN nanolayers

HEAs	Fe (at%)	Mn (at%)	Co (at%)	Cr (at%)	Ni (at%)
FMCC	48.80	27.28	12.42	11.50	–
FMCN	50.06	28.68	11.55	–	9.71

the HEA layers as a whole is greater than that of traditional pure metal NLs, which could attribute to the HEAs themselves with the unique microstructure and the severe lattice distortion. The phase transformation occurs in Cu/HEA NLs with large h, whose strengthening capability is apparently higher than those NLs without phase transformation. Thus, the strengthening capability of Cu/FMCC NLs with stress-induced transformation is much better than that of Cu/FMCN ones, indicating that the phase transformation provides extra strengthening.

DISCUSSION

Phase structure evolution in the as-deposited HEA nanolayers

The bulk FMCC HEA contains a duplex microstructure of HCP and FCC phases [11], while the bulk FMCN sample presents a single FCC phase, which is mostly consistent with the phase

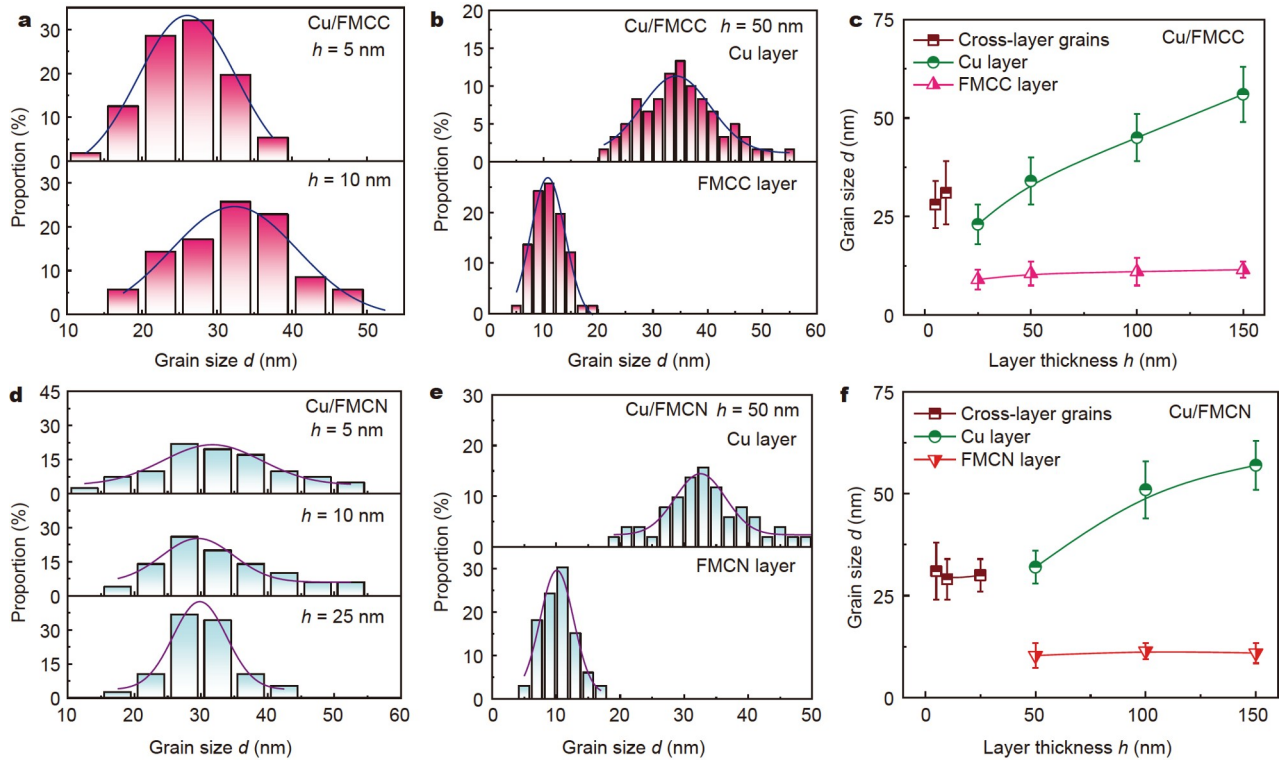

Figure 4 (a) Cross-layer grain size histograms for Cu/FMCC NLs with h = 5 and 10 nm. (d) Cross-layer grain size histograms for Cu/FMCN NLs with h = 5, 10 and 25 nm. (b, e) Grain size histograms of Cu and HEA layers for Cu/FMCC and Cu/FMCN NLs, respectively. (c, f) Average grain size as a function of layer thickness for Cu/FMCC and Cu/FMCN NLs, respectively.

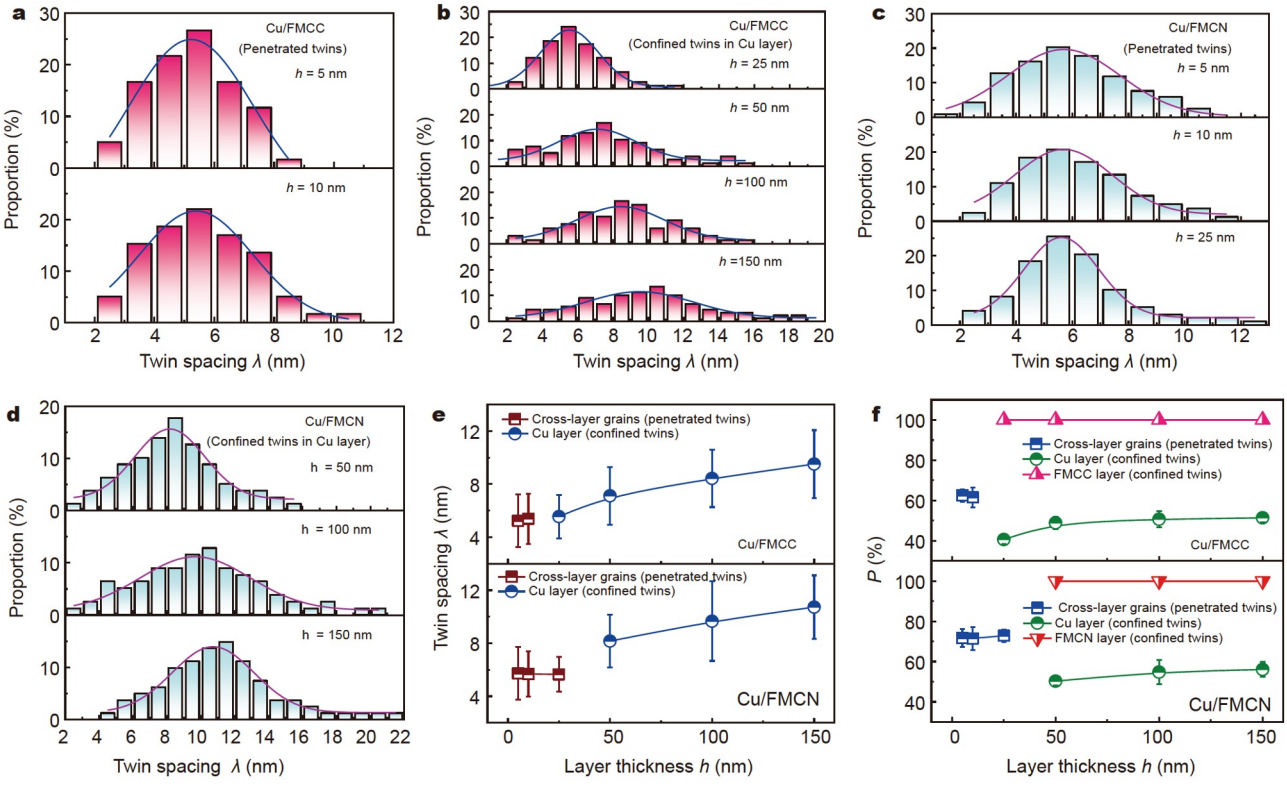

Figure 5 Histograms of penetrated twin spacing in the cross-layer grains of (a) Cu/FMCC and (c) Cu/FMCN NLs. Histograms of confined twin spacing in the Cu layers of (b) Cu/FMCC and (d) Cu/FMCN NLs. (e) Average twin spacing and (f) the fraction of grains with nanotwins as a function of layer thickness h for the present Cu/HEA NLs.

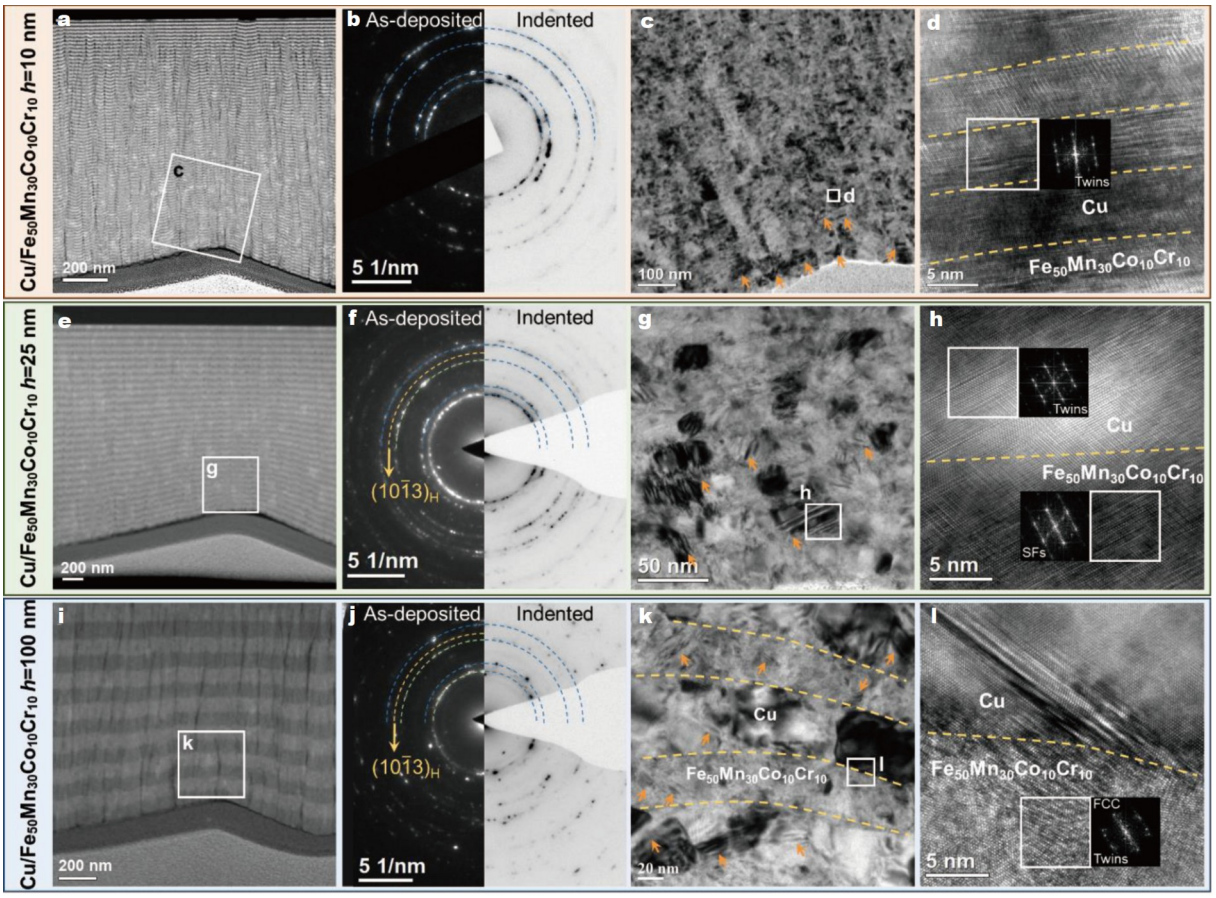

Figure 6 Representative images of the deformed microstructure underneath the indenter in Cu/FMCC NLs with (a–d) h = 10 nm, (e–h) h = 25 nm and (i–l) h = 100 nm. (a, e, i) Representative STEM images of the deformed region. (b, f, j) Typical SADPs of the as-deposited sample on the left side and the severe deformed sample on the right side. (c, g, k) Magnified TEM images of the boxed region in (a, e, i), and nanotwins are marked by orange arrows. (d, h, l) Typical HRTEM images of the severe deformed region boxed in (c, g, k).

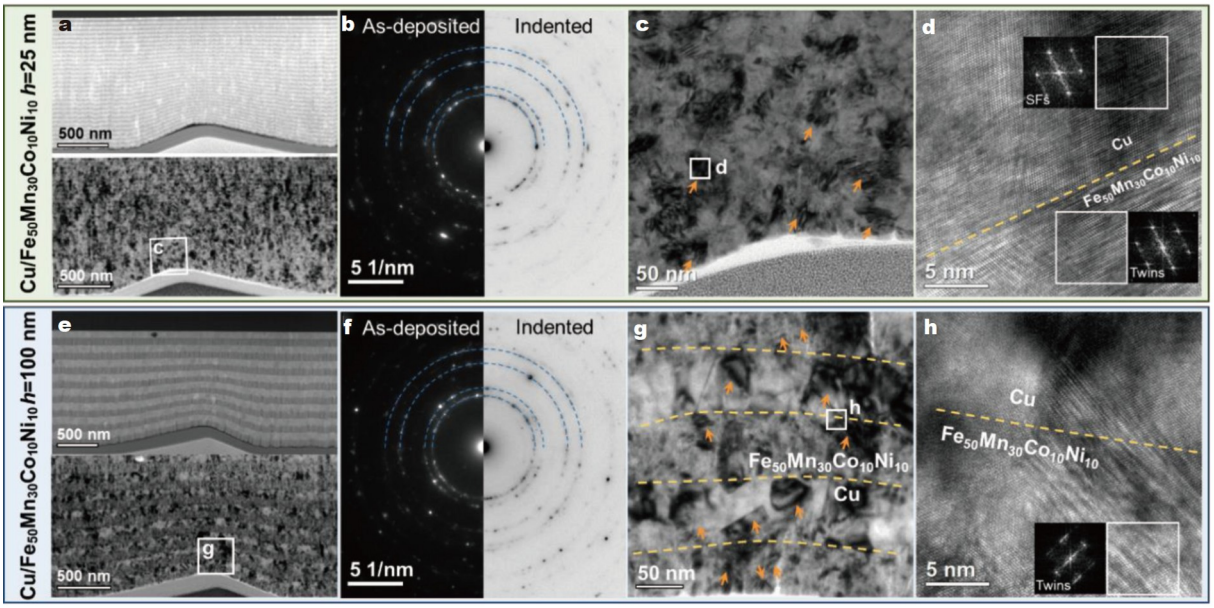

Figure 7 Representative images of the deformed microstructure underneath the indenter in Cu/FMCN NLs with (a–d) h = 25 nm. and (e–h) h = 100 nm. (a, e) Representative STEM images and bright field TEM images of the deformed region. (b, f) Typical SADPs of the as-deposited sample on the left side and the server deformed sample on the right side. (c, g) Magnified TEM images of the boxed region in (a, e), and nanotwins are marked by orange arrows. (d, h) Typical HRTEM images of the severe deformed region boxed in (c, g).

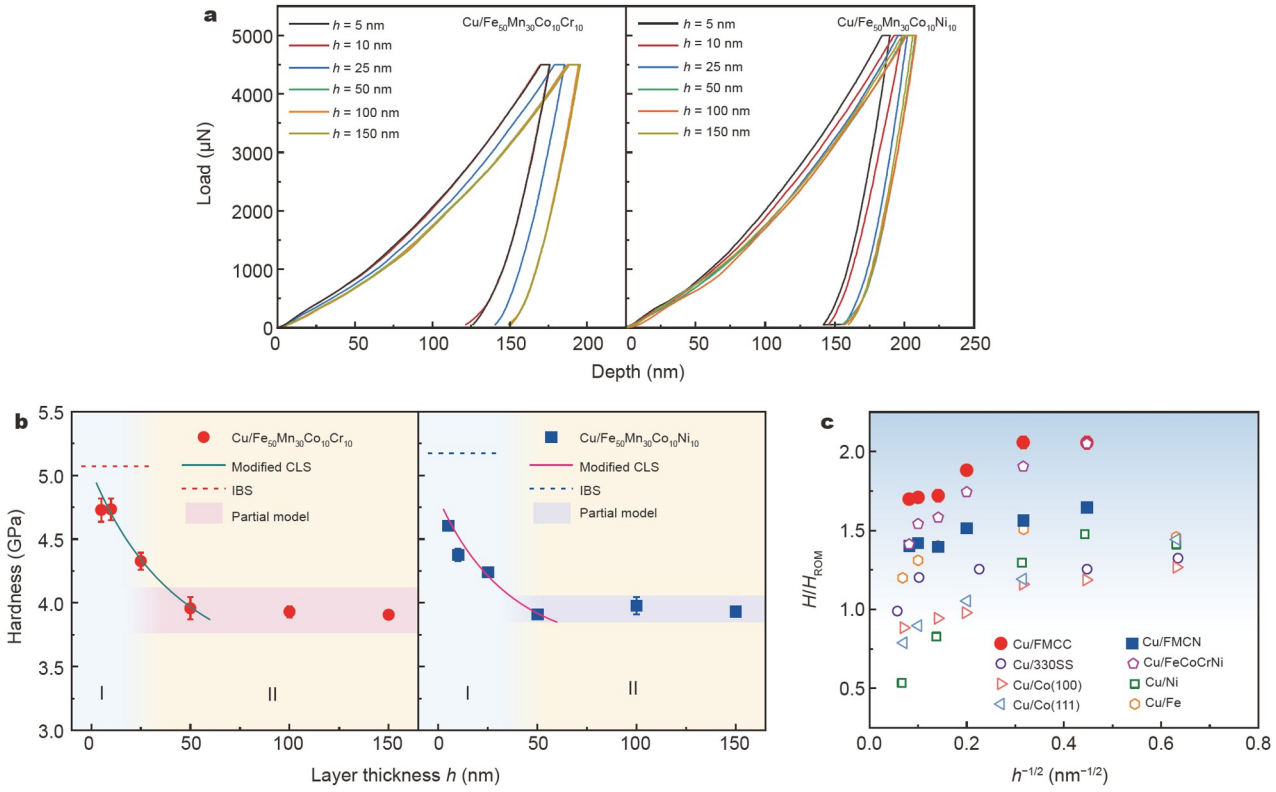

Figure 8 (a) Representative load-depth curves of Cu/FMCC and Cu/FMCN NLs with different h. (b) Dependence of nanoindentation hardness on h for both Cu/HEA NLs. (c) The parameter H/H_{ROM} as a function of the present Cu/HEA NLs, compared with the reported bimetal multilayers [33,35,44–46].

structure of the as-deposited HEA nanolayers in NLs. In the present Cu/HEA NLs with small h in Regime-I, their characteristic sizes are the domain grain sizes of ~30 nm, which are too large for phase transformation in NLs. While in Regime-II, the grain sizes in HEA layers become ~10 nm, making it possible for phase transformation. Under the strong constraining effect, the constituents are more favorable for phase transformation. For example, the phase transformation in NLs was observed in several bimetal systems when layer thickness h was reduced to a few nanometers, such as Ti/Nb [31], Zr/Nb [47], Cu/Fe [46] and Al/Ti [48]. In particular, for the present Cu/HEA NLs, the Cu layers play a role of "template" in the deposition process and then significantly affect the microstructure of HEA layers. This template effect has been employed to introduce a high-density of nanotwins in high-SFE metal Al through incorporating a buffer layer of a low-SFE metal Ag [49]. Moreover, the template layers with different orientations would generate different structures of NLs. For example, in the (100) textured Cu/Co NLs deposited on the Si(100) substrate, Co showed a primarily FCC structure, whereas in the (111) textured system on the Si(110) substrate, Co displayed a mixture of FCC and HCP phases at large h [45]. With reducing h, the Cu template effect increases, associated with the increased constraining effect. In this regard, the present Cu layers with an FCC structure introduce the FCC phase into FMCC nanolayers through the epitaxial growth, thereby forming FCC/FCC Cu/FMCC NLs with small h in Regime-I and Cu/dual-phase FMCC NLs with large h in Regime-II. Similarly, the template effect of Cu renders the FMCN nanolayers in Cu/FMCN NLs only show the FCC single phase structure, forming FCC/FCC Cu/FMCN NLs, regardless of h. At the same time, the formation of abundant SFs/nanotwins can effectively release the strain energy of the system, in particular at small h, as revealed in NLs of Cu/Ni [33] and Cu/Co [45].

Stress-driven phase transformation in deformed HEA nanolayers

The stress-driven phase transformation has been uncovered in some materials, such as HEAs [11,12], steels [10], and Ti-based alloys [50], which confers these materials outstanding mechanical properties. Actually, its premise is that there must be nuclei for the phase transformation. For example, the lamella HCP phase in the BCC $Ta_{0.5}HfZrTi$ HEAs acts as the transformation nuclei and then multiplies and coarsens with further deformation [12]. Another example is that SFs in stainless steels act as the martensitic embryos, and the martensite extends through dislocation gliding, resulting in the phase transformation from FCC austenite to HCP martensite during deformation [10]. More specifically, the high Mn segregation on the decorated martensite boundaries promotes the heterogeneous nucleation of austenite in the Fe-9 at% Mn steel [51]. Then, we will discuss the different transformation behaviors of HEAs based on this premise.

Previous studies showed that FeMnCoCrNi HEAs behaved the stress-driven FCC-to-HCP transformation [11,14], as well as the reverse HCP-to-FCC transformation [16,52]. The underlying reasons are as follows [16]: the thermal transformation barriers of these two phases that have nearly the same stability are very small on the one hand, and the dynamic forward and backward transformations can be realized by the motion of Shockley partials on the other hand. Moreover, based on the elaborated atomistic simulations, Lu *et al.* [16] and Fang *et al.* [52] also pointed out that the FCC-to-HCP phase transformation in FeCoCrNiMn HEAs could be realized by the dissociation of the

full dislocations and the HCP-to-FCC phase transformation by the association of the Shockley partials. In other words, the back and forth movement of the same Shockley partials results in the reversible HCP-to-FCC transformation with the preservation of the orientation.

For the present Cu/FMCC NLs, the FCC phase and SFs in the as-deposited FMCC nanolayers provide nuclei for the formation of FCC phase transformed from the HCP phase, leading to the stress-induced HCP-to-FCC transformation during indentation deformation. The HCP/FCC phase boundary with high energy often promotes the phase transformation, owing to their inner energy with the relatively small barrier for the HCP-to-FCC transformation [16,52]. In particular, under the strong constraining conditions, one constituent is more preferred to transform to form fully coherent interface with the other constituent to lower the heterogeneous interface energy of Cu/FMCC NLs, in agreement with previously reported results, including Ti/Nb [31], Zr/Nb [47], and Cu/Fe [46]. By contrast, only FCC phase emerges in FMCN nanolayers of the as-deposited Cu/FMCN NLs, owing to the combination of size constraining effect and Cu template effect. During the subsequent indentation deformation, the coherent interface in Cu/FMCN NLs with very low energy does not facilitate phase transformation on the one hand [30], but enables continuous slip of dislocations to transmit across the coherent interface on the other hand [53]. In this case, once the Shockley partial emitted from the boundary/interface along the slip plane creates an SF in the FCC phase in FMCN nanolayers with low SFE (compared with Cu), the SF can serve as an embryo of a nanotwin and becomes thicken *via* the subsequent gliding of twinning partials [54]. Such a process not only renders the breakdown of stress-induced HCP-to-FCC transformation, but also gives rise to the formation of abundant nanotwins in Cu/FMCN NLs, as verified in Fig. 7.

Twinning behavior in Cu/HEA NLs

It was reported that the HCP-FCC phase transformation was in favor of facilitating the deformation twinning [55–57]. The HCP-FCC phase transformation can be achieved by the movement of $a/6$ <112> Shockley partial dislocations on alternated {111}-planes [16], while the deformation twinning usually occurs *via* continuous gliding of partial dislocations on consecutive {111}-planes [55]. The HCP is characterized by the easy slips of partials on the basal planes, which leads to the FCC twin platelets and more twin boundaries (TBs) during deformation, further enhancing the prosperity of twins. Furthermore, the interface, especially coherent interface, could facilitate the deformation twining [58] or detwinning [34]. During deformation, partial dislocations emit from the interface and glide into the constituent layers, then affect the twinning behavior. In this work, nanotwins in both Cu and HEA layers are stable during deformation, regardless of h, see Figs 6 and 7. However, a prior study showed that detwinning occurred in coherent Cu/FeCoCrNi [35]. For Cu/FeCoCrNi NLs with small h, nanotwins penetrated across the interfaces, and provided channels for partials nucleating in Cu layers and sliding across the interfaces easily, leading to detwinning in both Cu and FeCoCrNi layers. For those with large h, nanotwins were confined into isolated layers and partials in Cu must constrict into full dislocations to transmit interfaces, rendering detwinning only occurs in Cu rather than FeCoCrNi layers [35]. It is suggested that the evolution of nanotwins during deformation in Cu/FeCoCrNi NLs is strongly influenced by the stability of nanotwins in Cu layers.

In fact, the twin spacing λ plays a vital role in the evolution of nanotwins during deformation [59]. There is a critical twin spacing λ_{cri} for the transition from TB hardening to TB softening [59,60]. When λ is larger than λ_{cri}, the strength increases with decreasing λ, which is well explained by the Hall–Petch (H–P) strengthening relationship, since TBs can serve as barriers to dislocation gliding, as given by [61],

$$\sigma_{\text{T-hardening}} = \sigma_0 + k \cdot \lambda^{-1/2}. \tag{1}$$

While as λ further decreases down to below λ_{cri}, the softening behavior occurs, which could be ascribed to the plastic deformation dominated by TB migration. The partials nucleate from GB-TB intersections and then glide along the twin planes, resulting in TB migration, i.e., detwinning. In this case, the strength of a material contributed by nanotwins can be expressed as [60],

$$\sigma_{\text{T-softening}} = M\left[\frac{\Delta U}{SV^*} - \frac{k_B T}{SV^*}\ln\left(\frac{d}{\lambda}\frac{v_D}{\dot{\varepsilon}}\right)\right], \tag{2}$$

where M is the Taylor factor, ΔU is the activation energy, S is a factor representing local stress concentration and geometry, V^* is the activation volume, k_B is the Boltzmann constant, T is the Kelvin temperature, d is the grain size, v_D is the Debye frequency, and $\dot{\varepsilon}$ is the macroscopic strain rate. The first term can be regarded as the athermal resistance and the second term is due to thermal softening. In this model applied to the present Cu/HEA NLs, ΔU and S are adjustable, while other parameters are fixed. The adjustable ΔU and S of the Cu layers are related to the coherent strain of interfaces. The higher the stress level, the lower the activation energy [62]. Thus, a possible reason for the discrepancy between the reported Cu/FeCoCrNi and the present Cu/HEA NLs is that λ of Cu layers is smaller than its λ_{cri}, making it possible to detwin in the former. However, λ of Cu layers in the latter is larger than its λ_{cri}, and thus the nanotwins are stable and play an important role in strengthening rather than softening of materials.

Strengthening mechanisms of Cu/HEA NLs

Strengthening mechanisms of Cu/HEA NLs in the Regime-I

It is well-known that material properties are controlled by the microstructure, which also influences the deformation mechanisms. The size effect on strengthening in conventional bimetal NLs has been extensively investigated and well captured by several strengthening models operative at different length scales, such as the classical Hall–Petch model, the confined layer slip (CLS) model and the interface barrier strength (IBS) model [32]. In the nanoscale, whether the CLS model works in the NLs depends on the magnitude of the IBS. Once the stress needed for hairpin dislocations gliding in isolated layers overwhelms the IBS, the deformation mechanism changes from CLS to dislocation transmission. Thus, we first calculate the IBS of Cu/HEA NLs *via* the following equation [45]:

$$\sigma_{\text{IBS}} = \sigma_K + \sigma_d + \sigma_{ch} = M\mu^* R\frac{\sin\varphi}{8\pi} + M\beta\mu^*\left(\varsigma - \frac{b}{L}\right) + M\frac{\Delta\gamma}{b}, \tag{3a}$$

where σ_K is Koehler stress originating from modulus mismatch, σ_d is determined by misfit dislocations due to lattice mismatch

which could be neglected considering the coherent interfaces in Cu/HEA NLs, and σ_{ch} is chemical interaction term related to the SFE difference between constituents. The interfaces of Cu/HEA NLs are coherent without lattice mismatch, hence the interface strength can be given by

$$\sigma_{IBS} \approx M\mu^* R\frac{\sin\varphi}{8\pi} + M\frac{\Delta\gamma}{b}, \tag{3b}$$

where M is Taylor factor, $\mu^* = \frac{2\mu_{Cu}\mu_{HEA}}{\mu_{Cu}+\mu_{HEA}}$ is the mean shear modulus, $R = \frac{\mu_{HEA}-\mu_{Cu}}{\mu_{HEA}+\mu_{Cu}}$, φ is the angle between the slip plane and interface, $\Delta\gamma = \gamma_{Cu} - \gamma_{HEA}$ is the SFE difference and b is the magnitude of the Burgers vector. Previous study [63] has revealed that the dislocations nucleated from GBs converted from partials to full dislocations at a critical size d_{cri}, which was ~128 nm for Cu and larger than the grain size in this regime. Hence, it is the partials nucleating in Cu layers that govern the deformation mechanism in Cu/HEA NLs. Taking M = 3, μ_{Cu} = 48.3 GPa [45], μ_{FMCC} = 80 GPa [64], μ_{FMCN} = 77 GPa [65], φ = 70.5, γ_{Cu} = 41 mJ m^{-2} [45], γ_{FMCC} = 22 mJ m^{-2} [64], γ_{FMCN} = 31 mJ m^{-2} [64] (the SFE of FeMnCoCrNi alloy is similar in the range of 22–31 mJ m^{-2}), $b_{p,Cu}$ = 0.1476 nm, the estimated IBS is ~1.87 and ~1.91 GPa for Cu/FMCC and Cu/FMCN NLs, respectively. Their corresponding hardness is present in Fig. 8b as red and blue dot lines, respectively. Although the IBS is larger than the applied stress, the unique characteristic of coherent interfaces with the continuous slip system makes it easy for dislocations to transmit across the interface. On the other hand, the columnar grains in Regime-I provide another characteristic size, i.e., their domain grain sizes also play a critical role on dislocation slip. The dislocations emitted from GBs are confined inside the columnar grains by GBs to glide, following the CLS model. In this case, both of the grain size d and layer thickness h make remarkable effects on the strength, and thus the characteristic size should be expressed as $h_{eff} = (h + 2d)/3$ [66].

Misra *et al.* [32] proposed a refined CLS model considering the effect of dislocation core spreading along the interface, the interface stress and the resistance from interface dislocation arrays, as follows:

$$\sigma_{CLS} = \frac{M\mu b\sin\varphi}{8\pi h}\left(\frac{4-\nu}{1-\nu}\right)\ln\left(\frac{\alpha h}{b\sin\varphi}\right) - \frac{F}{h} + \frac{\mu f\varepsilon}{B(1-\nu)}. \tag{4}$$

However, this model neglects the interactions between nanotwins and partials as well as the SFE effect on gliding partials. Actually, the contributions of these two factors should be included in the modified CLS model, yielding

$$\sigma_X = \frac{M\mu b_p\sin\varphi}{8\pi h_{eff}}\left(\frac{4-\nu}{1-\nu}\right)\ln\left(\frac{\alpha h_{eff}}{b_p\sin\varphi}\right) - \frac{F}{h} + \frac{\mu f\varepsilon}{B(1-\nu)} + Pk_T\lambda^{-1/2} + (1-P)M\left(\frac{\gamma}{b_p}\right), \tag{5}$$

where α represents the core cut-off parameter, ν is the Poisson's ratio, F is the characteristic interface stress of NLs, f is volume fraction of constituent layers, ε is the in-plane plastic strain, B is a strain resolution factor of the order of 0.5 for the active slip system, and k_T is a constant. Considering the feature of severe distortion in HEAs, the lattice friction σ_0 cannot be ignored as a strengthening factor. The lattice friction can be predicted based on the motion of dislocation through the HEAs [67]. The zero-temperature shear stress τ_0 and the energy barrier ΔE_b for thermally activated flow are given by

$$\tau_0 = A_\tau\chi^{-\frac{1}{3}}\mu\left[\frac{1+\nu}{1-\nu}\right]^{\frac{4}{3}}\left[\frac{\Sigma_n c_n\Delta V_n^2}{b^6}\right]^{\frac{2}{3}}, \tag{6}$$

$$\Delta E_b = A_E\chi^{\frac{1}{3}}\mu b^3\left[\frac{1+\nu}{1-\nu}\right]^{\frac{2}{3}}\left[\frac{\Sigma_n c_n\Delta V_n^2}{b^6}\right]^{\frac{1}{3}}. \tag{7}$$

At finite temperature T and strain rate $\dot{\varepsilon}$, the predicted lattice frication σ_0 is expressed as

$$\sigma_0(T,\dot{\varepsilon}) = M\tau_0\left[1 - \left(\frac{k_B T}{\Delta E_b}\ln\frac{\dot{\varepsilon}_0}{\dot{\varepsilon}}\right)^{\frac{2}{3}}\right]. \tag{8}$$

The prefactor coefficients A_τ and A_E emerge from the reduced elasticity theory and depend on the solute misfit volumes and dislocation pressure field, which are 0.01785 and 1.5618, respectively, stemming from the calculation of the typical atomistic structure of FCC dislocation [67]. χ is related to the edge dislocation line tension which is 0.125 for FCC alloys [68]. $\Delta V_n = V_n - V_{HEA}$ is the misfit volume of the n-component HEAs, and $V_{HEA} = \Sigma_n c_n V_n$, where c_n is the atomic content of each element and V_n is the apparent volume of the constituent elements. $\dot{\varepsilon}_0 = 10^4$ s^{-1} is a reference strain rate and $\dot{\varepsilon} = 0.1$ s^{-1} is the macroscopic strain rate of the present nanoindentation. k_B is the Boltzman constant of ~1.38 × 10^{23} J K^{-1}, and T is the temperature ~298 K. Taking μ_{FMCC} = 80 GPa [64], μ_{FMCN} = 77 GPa [65], ν_{FMCC} = 0.28 [64], ν_{FMCN} = 0.28 [64], $b_{f,FMCC}$ = 0.2531 nm [64], $b_{f,FMCN}$ = 0.2539 nm [64], c_n = (0.5, 0.3, 0.1, 0.1), and V_n = (12.09, 12.60, 11.12, 12.27, 10.94) Å^3 [67] for Fe, Mn, Co, Cr and Ni, respectively, the lattice friction σ_0 for FMCC HEA is ~65.8 MPa and for FMCN HEA is ~105.5 MPa. In addition, the lattice friction σ_0 for Cu is ~25.5 MPa [69]. Therefore, the CLS model can be modified as follows:

$$\sigma_X = \sigma_0 + \frac{M\mu b_p\sin\varphi}{8\pi h_{eff}}\left(\frac{4-\nu}{1-\nu}\right)\ln\left(\frac{\alpha h_{eff}}{b_p\sin\varphi}\right) - \frac{F}{h} + \frac{\mu f\varepsilon}{B(1-\nu)} + Pk_T\lambda^{-1/2} + (1-P)M\left(\frac{\gamma}{b_p}\right). \tag{9}$$

Giving the Cu/HEA NLs show synergistic deformation behavior, we approximately estimate the strength of the NLs by ROM as follows [70]:

$$\sigma = \xi_{Cu}\cdot\sigma_{Cu} + \xi_{HEA}\cdot\sigma_{HEA}, \tag{10}$$

where ξ_{Cu} and ξ_{HEA} are the deformed fraction contribution of Cu and HEA layers, representatively, which could be taken as an equal value of 0.5 for the sake of simplicity. Taking ν_{Cu} = 0.343, $b_{p,FMCC}$ = 0.1461 nm [64], $b_{p,FMCN}$ = 0.1466 nm [64], α = 0.8, $\varepsilon_{Cu/FMCC}$ = 0.03%, $\varepsilon_{Cu/FMCN}$ = 0.25%, F = 2.0 J m^{-2}, k_T = 3.4 GPa nm$^{1/2}$ [61], $P_{Cu/FMCC}$ = 61%, $P_{Cu/FMCC}$ = 72%, $\lambda_{Cu/FMCC}$ = 5.2 nm, $\lambda_{Cu/FMCN}$ = 5.4 nm, then substituting Equation (9) to Equation (10), the corresponding hardness of the calculated strength agrees well with the experimental results, as shown in Fig. 8b by the green and pink solid lines for Cu/FMCC and Cu/FMCN NLs, respectively. However, this model far underestimates the strength of Cu/HEA NLs with large h in Regime-II. There should be other mechanisms contributing to their mechanical response at such length scale, as discussed below.

Strengthening mechanisms of Cu/HEA NLs in Regime-II

In general, the hardness/strength of NLs at large h is often

captured by the H–P relationship, showing smaller h leads to higher hardness/strength. However, the size h-independent hardness implies that the H–P relationship is breakdown in Regime-II for the present Cu/HEA NLs. Actually, the deformation mechanisms of metals may vary with grain size d. When d is in the range of micro- to submicron-scale, the dislocations generate in grain interiors and then move towards boundaries, and thus the strength is determined by the stress needed to overcome the obstructions during gliding, such as GBs and TBs. When d is reduced into the nanoscale, it is quite difficult for dislocations to generate in grain interiors, and thus the stress needed for dislocations emission from GBs becomes the controlling factor of strength [71]. When d further reduces to ~15 nm or even less, the deformation mainly stems from the GB-mediated mechanisms, such as grain rotation and GB sliding, leading to the reverse H–P effect [72].

Obviously, the GB-mediated mechanism does not work in the present Cu/HEA NLs owing to the strong layer constraining effect, and it is easier for dislocations to generate and slip in Cu layers owing to their relatively larger grain sizes. In fact, the small grain size in HEA layers makes it difficult for partials emitting rather than gliding, thus the strength of Cu/HEA NLs can be regarded as the critical stress for partial emission in HEA layers. Therefore, the critical stress could be predicted by [73–75],

$$\sigma_{\text{Partial}} = \frac{1}{ms}\left(\frac{2\beta\mu b_{\text{p}}}{d} + \frac{\gamma}{b_{\text{p}}}\right), \tag{11}$$

where m is a stress concentration factor of 2–4 [75], s is the Schmid factor of the corresponding slip system of 0.27–0.41 [73], and β is the order of unity, reflecting the character of a dislocation [74]. The in-plane columnar grain size d of HEA layers in Regime-II is ~9.8–12.1 and ~10.3–10.9 nm for Cu/FMCC and Cu/FMCN NLs, respectively. Taking m = 2, s = 0.41 and other parameters have the same meaning as above, the corresponding hardness from the calculated σ_{partial} is depicted as the light pink and light blue region for Cu/FMCC and Cu/FMCN NLs in Fig. 8b, respectively. It is found that the experimental data fall into this region, implying the mechanism of partial emission from interfaces/boundaries in HEA nanolayers is activated. Moreover, the corresponding hardness from the calculated σ_{partial} for Cu layers is obviously h-dependent in the range of ~1.98–2.81 GPa, which is much lower than the hardness of Cu/HEA NLs, and thus it is not the determining mechanism.

CONCLUSIONS

In this study, we systematically investigated the phase transformation behaviors of two kinds of Cu/HEA NLs with different layer thicknesses, i.e., Cu/FMCC and Cu/FMCN NLs, in terms of microstructural evolution and mechanical properties. The current work provides a new pathway to tailor the stress-induced phase transformation and thereby synthesize high-strength metallic materials. Three main conclusions are summarized as follows.

(1) The size-driven HCP-to-FCC phase transformation appeared in FMCC HEA nanolayers with reducing h during the non-equilibrium magnetron sputtering, while the FMCN nanolayers displayed h-independent single FCC phase same as the bulk sibling. The Cu layers in Cu/HEA NLs played a role of template and introduced the FCC phase into HEA layers.

(2) The stress-driven HCP-to-FCC phase transformation occurred in the dual-phase FMCC layers with large h, due to their interfacial structure and layer constraining effect. However, the FMCN nanolayers in the as-deposited NLs maintained their initial single FCC phase structure during plastic deformation, ascribing to the coherent interface with very low energies.

(3) Owing to the high interface barrier, the dislocation sliding in the confined isolated nanolayers was the dominant deformation mechanism of Cu/HEA NLs associated with the nanotwin strengthening at small h. Within the large h range, the critical stress for partial emission in HEA layers became the controlling factor of ultrahigh hardness/strength due to the tiny grains in HEA nanolayers.

Received 14 August 2023; accepted 18 September 2023; published online 13 October 2023

1 Ritchie RO. The conflicts between strength and toughness. Nat Mater, 2011, 10: 817–822
2 Wang X, De Vecchis RR, Li C, *et al.* Design metastability in high-entropy alloys by tailoring unstable fault energies. Sci Adv, 2022, 8: eabo7333
3 Zhang Y, Zuo TT, Tang Z, *et al.* Microstructures and properties of high-entropy alloys. Prog Mater Sci, 2014, 61: 1–93
4 Guo L, Gu J, Gong X, *et al.* CALPHAD aided design of high entropy alloy to achieve high strength *via* precipitate strengthening. Sci China Mater, 2020, 63: 288–299
5 Li Z, Zhao S, Ritchie RO, *et al.* Mechanical properties of high-entropy alloys with emphasis on face-centered cubic alloys. Prog Mater Sci, 2019, 102: 296–345
6 Yang C, Ren C, Jia Y, *et al.* A machine learning-based alloy design system to facilitate the rational design of high entropy alloys with enhanced hardness. Acta Mater, 2022, 222: 117431
7 Liu J, Guo X, Lin Q, *et al.* Excellent ductility and serration feature of metastable CoCrFeNi high-entropy alloy at extremely low temperatures. Sci China Mater, 2019, 62: 853–863
8 Lu W, Guo W, Wang Z, *et al.* Advancing strength and counteracting embrittlement by displacive transformation in heterogeneous high-entropy alloys containing sigma phase. Acta Mater, 2023, 246: 118717
9 Cantor B. Multicomponent high-entropy Cantor alloys. Prog Mater Sci, 2021, 120: 100754
10 Mao W, Gao S, Gong W, *et al.* Quantitatively evaluating respective contribution of austenite and deformation-induced martensite to flow stress, plastic strain, and strain hardening rate in tensile deformed TRIP steel. Acta Mater, 2023, 256: 119139
11 Li Z, Pradeep KG, Deng Y, *et al.* Metastable high-entropy dual-phase alloys overcome the strength-ductility trade-off. Nature, 2016, 534: 227–230
12 Huang H, Wu Y, He J, *et al.* Phase-transformation ductilization of brittle high-entropy alloys *via* metastability engineering. Adv Mater, 2017, 29: 1701678
13 Ma Y, Yang M, Yuan F, *et al.* Deformation induced hcp nano-lamella and its size effect on the strengthening in a CoCrNi medium-entropy alloy. J Mater Sci Tech, 2021, 82: 122–134
14 Lin Q, Liu J, An X, *et al.* Cryogenic-deformation-induced phase transformation in an FeCoCrNi high-entropy alloy. Mater Res Lett, 2018, 6: 236–243
15 Vakili SM, Zarei-Hanzaki A, Anoushe AS, *et al.* Reversible dislocation movement, martensitic transformation and nano-twinning during elastic cyclic loading of a metastable high entropy alloy. Acta Mater, 2020, 185: 474–492
16 Lu W, Liebscher CH, Dehm G, *et al.* Bidirectional transformation enables hierarchical nanolaminate dual-phase high-entropy alloys. Adv Mater, 2018, 30: 1804727
17 Li Z, Tasan CC, Pradeep KG, *et al.* A TRIP-assisted dual-phase high-entropy alloy: Grain size and phase fraction effects on deformation behavior. Acta Mater, 2017, 131: 323–335
18 Vorobiov S, Pylypenko O, Bereznyak Y, *et al.* Magnetic properties,

magnetoresistive, and magnetocaloric effects of AlCrFeCoNiCu thin-film high-entropy alloys prepared by the co-evaporation technique. Appl Phys A, 2021, 127: 179
19 Cao ZH, Cai YP, Sun C, *et al.* Tailoring strength and plasticity of Ag/Nb nanolaminates *via* intrinsic microstructure and extrinsic dimension. Int J Plast, 2019, 113: 145–157
20 Ovid'Ko IA. Review on the fracture processes in nanocrystalline materials. J Mater Sci, 2007, 42: 1694–1708
21 Meyers MA, Mishra A, Benson DJ. Mechanical properties of nanocrystalline materials. Prog Mater Sci, 2006, 51: 427–556
22 Fu Z, Chen W, Wen H, *et al.* Microstructure and strengthening mechanisms in an FCC structured single-phase nanocrystalline $Co_{25}Ni_{25}Fe_{25}Al_{7.5}Cu_{17.5}$ high-entropy alloy. Acta Mater, 2016, 107: 59–71
23 Wu G, Chan KC, Zhu L, *et al.* Dual-phase nanostructuring as a route to high-strength magnesium alloys. Nature, 2017, 545: 80–83
24 Yang Z, Fu B, Ning Z, *et al.* Amorphization activated by semicoherent interfaces of FCC/BCC HEA multilayers during deformation. Mater Des, 2023, 225: 111469
25 Beyerlein IJ, Demkowicz MJ, Misra A, *et al.* Defect-interface interactions. Prog Mater Sci, 2015, 74: 125–210
26 Fan Z, Xue S, Wang J, *et al.* Unusual size dependent strengthening mechanisms of Cu/amorphous CuNb multilayers. Acta Mater, 2016, 120: 327–336
27 Jain M, Yaddanapudi K, Kidigannappa AT, *et al.* Simultaneous high strength and mechanical stability of bcc Nb/Mg nanolaminates. Acta Mater, 2023, 242: 118487
28 Wan Q, Liu Y, Yang B, *et al.* Enhancing irradiation tolerance *via* building 3D diffusion paths for He+ in multilayers by epitaxial growth. Mater Des, 2022, 221: 111020
29 Zhang YF, Su R, Niu TJ, *et al.* Thermal stability and deformability of annealed nanotwinned Al/Ti multilayers. Scripta Mater, 2020, 186: 219–224
30 Li JC, Liu W, Jiang Q. Bi-phase transition diagrams of metallic thin multilayers. Acta Mater, 2005, 53: 1067–1071
31 Wan L, Yu X, Thompson GB. Phase stability and *in situ* growth stresses in Ti/Nb thin films. Acta Mater, 2014, 80: 490–497
32 Misra A, Hirth JP, Hoagland RG. Length-scale-dependent deformation mechanisms in incoherent metallic multilayered composites. Acta Mater, 2005, 53: 4817–4824
33 Liu Y, Bufford D, Wang H, *et al.* Mechanical properties of highly textured Cu/Ni multilayers. Acta Mater, 2011, 59: 1924–1933
34 Zhao YF, Zhang JY, Wang YQ, *et al.* Unusual plastic deformation behavior of nanotwinned Cu/high entropy alloy FeCoCrNi nanolaminates. Nanoscale, 2019, 11: 11340–11350
35 Zhao YF, Feng XB, Zhang JY, *et al.* Tailoring phase transformation strengthening and plasticity of nanostructured high entropy alloys. Nanoscale, 2020, 12: 14135–14149
36 Wang Y, Liu B, Yan K, *et al.* Probing deformation mechanisms of a FeCoCrNi high-entropy alloy at 293 and 77 K using *in situ* neutron diffraction. Acta Mater, 2018, 154: 79–89
37 Zhao S, Stocks GM, Zhang Y. Stacking fault energies of face-centered cubic concentrated solid solution alloys. Acta Mater, 2017, 134: 334–345
38 Yang H, Zhu L, Zhang R, *et al.* Influence of high stacking-fault energy on the dissociation mechanisms of misfit dislocations at semi-coherent interfaces. Int J Plast, 2020, 126: 102610
39 Zhang YH, Zhuang Y, Hu A, *et al.* The origin of negative stacking fault energies and nano-twin formation in face-centered cubic high entropy alloys. Scripta Mater, 2017, 130: 96–99
40 Deng Y, Tasan CC, Pradeep KG, *et al.* Design of a twinning-induced plasticity high entropy alloy. Acta Mater, 2015, 94: 124–133
41 Gao Q, Gong M, Wang Y, *et al.* Phase transformation and properties of Fe-Cr-Co alloys with low cobalt content. Mater Trans, 2015, 56: 1491–1495
42 Oliver WC, Pharr GM. An improved technique for determining hardness and elastic modulus using load and displacement sensing indentation experiments. J Mater Res, 1992, 7: 1564–1583
43 Xue S, Fan Z, Lawal OB, *et al.* High-velocity projectile impact induced 9R phase in ultrafine-grained aluminium. Nat Commun, 2017, 8: 1653
44 Zhang X, Misra A, Wang H, *et al.* Enhanced hardening in Cu/330 stainless steel multilayers by nanoscale twinning. Acta Mater, 2004, 52: 995–1002
45 Liu Y, Chen Y, Yu KY, *et al.* Stacking fault and partial dislocation dominated strengthening mechanisms in highly textured Cu/Co multilayers. Int J Plast, 2013, 49: 152–163
46 Chen Y, Liu Y, Sun C, *et al.* Microstructure and strengthening mechanisms in Cu/Fe multilayers. Acta Mater, 2012, 60: 6312–6321
47 Thompson GB, Banerjee R, Dregia SA, *et al.* Phase stability of bcc Zr in Nb/Zr thin film multilayers. Acta Mater, 2003, 51: 5285–5294
48 Banerjee R, Dregia SA, Fraser HL. Stability of f.c.c. titanium in titanium/aluminum multilayers. Acta Mater, 1999, 47: 4225–4231
49 Bufford D, Liu Y, Zhu Y, *et al.* Formation mechanisms of high-density growth twins in aluminum with high stacking-fault energy. Mater Res Lett, 2013, 1: 51–60
50 Chen N, Kou H, Wu Z, *et al.* Design of metastable β-Ti alloys with enhanced mechanical properties by coupling αS precipitation strengthening and TRIP effect. Mater Sci Eng-A, 2022, 835: 142696
51 Raabe D, Sandlöbes S, Millán J, *et al.* Segregation engineering enables nanoscale martensite to austenite phase transformation at grain boundaries: A pathway to ductile martensite. Acta Mater, 2013, 61: 6132–6152
52 Fang Q, Chen Y, Li J, *et al.* Probing the phase transformation and dislocation evolution in dual-phase high-entropy alloys. Int J Plast, 2019, 114: 161–173
53 Chen W, Zhang J, Cao S, *et al.* Strong deformation anisotropies of ω-precipitates and strengthening mechanisms in Ti-10V-2Fe-3Al alloy micropillars: Precipitates shearing *vs* precipitates disordering. Acta Mater, 2016, 117: 68–80
54 Zhu YT, Liao XZ, Wu XL. Deformation twinning in nanocrystalline materials. Prog Mater Sci, 2012, 57: 1–62
55 Lu S, Sun X, Tian Y, *et al.* Theory of transformation-mediated twinning. PNAS Nexus, 2023, 2: pgac282
56 Chen Y, An X, Zhou Z, *et al.* Size-dependent deformation behavior of dual-phase, nanostructured CrCoNi medium-entropy alloy. Sci China Mater, 2021, 64: 209–222
57 Chen Y, Chen D, An X, *et al.* Unraveling dual phase transformations in a CrCoNi medium-entropy alloy. Acta Mater, 2021, 215: 117112
58 An XH, Zhu SM, Cao Y, *et al.* Atomic-scale investigation of interface-facilitated deformation twinning in severely deformed Ag-Cu nanolamellar composites. Appl Phys Lett, 2015, 107: 011901
59 Lu L, Chen X, Huang X, *et al.* Revealing the maximum strength in nanotwinned copper. Science, 2009, 323: 607–610
60 Li X, Wei Y, Lu L, *et al.* Dislocation nucleation governed softening and maximum strength in nano-twinned metals. Nature, 2010, 464: 877–880
61 Chen XH, Lu L, Lu K. Grain size dependence of tensile properties in ultrafine-grained Cu with nanoscale twins. Scripta Mater, 2011, 64: 311–314
62 Zhu T, Li J, Samanta A, *et al.* Temperature and strain-rate dependence of surface dislocation nucleation. Phys Rev Lett, 2008, 100: 025502
63 Asaro RJ, Suresh S. Mechanistic models for the activation volume and rate sensitivity in metals with nanocrystalline grains and nano-scale twins. Acta Mater, 2005, 53: 3369–3382
64 Liu SF, Wu Y, Wang HT, *et al.* Stacking fault energy of face-centered-cubic high entropy alloys. Intermetallics, 2018, 93: 269–273
65 Wu Z, Bei H, Pharr GM, *et al.* Temperature dependence of the mechanical properties of equiatomic solid solution alloys with face-centered cubic crystal structures. Acta Mater, 2014, 81: 428–441
66 Colla MS, Wang B, Idrissi H, *et al.* High strength-ductility of thin nanocrystalline palladium films with nanoscale twins: On-chip testing and grain aggregate model. Acta Mater, 2012, 60: 1795–1806
67 Varvenne C, Luque A, Curtin WA. Theory of strengthening in fcc high entropy alloys. Acta Mater, 2016, 118: 164–176
68 Yin B, Maresca F, Curtin WA. Vanadium is an optimal element for strengthening in both fcc and bcc high-entropy alloys. Acta Mater, 2020, 188: 486–491
69 Li XG, Cao LF, Zhang JY, *et al.* Tuning the microstructure and mechanical properties of magnetron sputtered Cu-Cr thin films: The op-

timal Cr addition. Acta Mater, 2018, 151: 87–99
70 Fan Z, Liu Y, Xue S, *et al.* Layer thickness dependent strain rate sensitivity of Cu/amorphous CuNb multilayer. Appl Phys Lett, 2017, 110: 161905
71 Van Swygenhoven H. Grain boundaries and dislocations. Science, 2002, 296: 66–67
72 Yip S. The strongest size. Nature, 1998, 391: 532–533
73 Gruber PA, Böhm J, Onuseit F, *et al.* Size effects on yield strength and strain hardening for ultra-thin Cu films with and without passivation: A study by synchrotron and bulge test techniques. Acta Mater, 2008, 56: 2318–2335
74 Chen M, Ma E, Hemker KJ, *et al.* Deformation twinning in nanocrystalline aluminum. Science, 2003, 300: 1275–1277
75 Zhang JY, Liu G, Wang RH, *et al.* Double-inverse grain size dependence of deformation twinning in nanocrystalline Cu. Phys Rev B, 2010, 81: 172104

Acknowledgements This work was supported by the National Natural Science Foundation of China (U2067219, 92163201, and 52001247), the Initiative Postdocs Supporting Program (BX20190266), Shaanxi Province Youth Innovation Team Project (22JP042), and the Fundamental Research Funds for the Central Universities (xtr022019004 and xzy022019071). We would thank Dr. Shengwu Guo, Yanhuai Li and Jiao Li for their kind help with the microstructural characterization of materials.

Author contributions Sun J and Liu G supervised the project. Wang Y and Zhang J initiated the research concept. Zhao Y and Wu K conducted the experiments. Wang Y and Zhang J interpreted the results and wrote the manuscript, with significant input from all other authors.

Conflict of interest The authors declare that they have no conflict of interest.

Yufang Zhao received her BSc degree from Xi'an Jiaotong University in 2016 and earned her PhD degree in 2022, under the supervision of Prof. Jun Sun at the College of Materials Science and Engineering, Xi'an Jiaotong University. She joined the North University of China in 2022. Her current research interest is the mechanical behavior of nanolaminates.

Yaqiang Wang obtained his BSc degree (2012) and PhD degree (2019) in materials science and engineering from Xi'an Jiaotong University. He joined Prof. Gang Liu's group after PhD graduation and was promoted to associate professor in 2021. His current research focuses on the deformation and fracture of nanostructured metal thin films/nanolaminates.

Jinyu Zhang earned his BSc degree (2005) from Lanzhou University of Technology and PhD degree (2011) in materials science and engineering from Xi'an Jiaotong University. He joined Prof. Gang Liu's group in 2012 and was promoted to professor in 2017. His research focuses on the strengthening & toughening and deformation of nanostructured metals.

Jun Sun obtained his BSc degree from Jilin University (1982) and PhD degree (1989) in materials science and engineering from Xi'an Jiaotong University. In 2002, he joined the State Key Laboratory for Mechanical Behavior of Materials at Xi'an Jiaotong University, where he is currently a professor and group leader. His research focuses on the multiscale effect of materials' deformation and transformation, and microstructure optimization and mechanical property enhancement of metals.

超强金属/高熵合金纳米叠层材料：利用相变的尺寸约束效应

赵宇芳, 王亚强*, 张金钰*, 吴凯, 刘刚, 孙军*

摘要 本文通过磁控溅射制备了具有相同组元层厚度(h = 5–150 nm)的Cu/$Fe_{50}Mn_{30}Co_{10}Cr_{10}$和Cu/$Fe_{50}Mn_{30}Co_{10}Ni_{10}$金属/高熵合金纳米多层膜，对比研究了强约束条件下非等原子比$Fe_{50}Mn_{30}Co_{10}Cr_{10}$和$Fe_{50}Mn_{30}Co_{10}Ni_{10}$高熵合金的相稳定性及其对力学性能的影响. 沉积过程中由于组元Cu层的约束与模板效应，组元$Fe_{50}Mn_{30}Co_{10}Cr_{10}$层在层厚小于25 nm时发生了尺寸驱动的HCP到FCC相变. 与此同时，由于堆垛层错可以作为相变的形核质点，Cu/$Fe_{50}Mn_{30}Co_{10}Cr_{10}$多层膜在压入变形过程中也发生了应力驱动的HCP到FCC相变. 相比之下，Cu/$Fe_{50}Mn_{30}Co_{10}Ni_{10}$多层膜组织稳定，没有发生尺寸/应力驱动的相变行为. 随层厚减小，两种Cu/高熵合金纳米多层膜均表现出了从层厚无关转变为层厚相关的超高硬度，这源于偏位错形核主导的强化机制. 尤为特别的是，Cu/$Fe_{50}Mn_{30}Co_{10}Cr_{10}$多层膜的归一化硬度(实测硬度与混合法则预测硬度的比值)远高于传统的Cu基双金属多层膜. 本文研究结果从调控高熵合金相变行为的角度为提高复合材料的强度和塑性提供了新思路.

